Magnetic chirality probed by polarized neutrons and neutron spin echo spectroscopy

Pappas, Catherine; Lelièvre-Berna, Eddy; Ehlers, Georg

DOI
10.1016/bs.hmm.2024.08.002

Publication date
2024

Document Version
Final published version

Published in
Handbook of Magnetic Materials

Chapter 1

Magnetic chirality probed by polarized neutrons and neutron spin echo spectroscopy

Catherine Pappas[a,*], and Eddy Lelièvre-Berna[b]
[a]*Faculty of Applied Sciences, Delft University of Technology, Delft, The Netherlands,* [b]*Institut Laue-Langevin, Grenoble, France*
[*]*Corresponding author. e-mail address: c.pappas@tudelft.nl*

Chapter Outline

1 Introduction

In the field of bulk chiral magnetism, helical, cycloidal or skyrmion lattice magnetic structures and textures have been to a great extend unravelled by neutron scattering. The focus has been on the members of the B20 family, which are spontaneously chiral like MnSi (see e.g. Grigoriev, 2005; Pappas et al., 2009; Kindervater et al., 2014) or on mutliferroic systems such as $MnWO_4$, where magnetic chirality is induced by applying electric fields (Finger et al., 2010a). In this topical field of research, where fundamental research is often driven by potential applications in spintronics (Fert et al., 2013; Sampaio et al., 2013), the scattering of polarized neutron beams has been an invaluable tool as it provides a direct and unique insight on the specific topology of magnetic correlations. This is due to the vector nature of the (dipole) interaction between the neutron beam polarization and a magnetic sample, which has been the subject of extensive literature (Halpern and Johnson, 1939; Blume, 1963; Maleyev, 1962, Maleyev et al.,

Handbook of Magnetic Materials, Vol. 33. https://doi.org/10.1016/bs.hmm.2024.08.002

1963; Brown, 2001; Simonet et al., 2012); since the pioneering experiment by O. Frisch et al., where for the first time a polarized neutron beam was produced and Larmor precessions were induced (Frisch et al., 1938).

In this review, we focus on the scattering of a polarized neutron beam by magnetic correlations only and will thus neglect any nuclear and nuclear magnetic interference contributions. Almost all previous work (see e.g. Brown, 2001; Simonet et al., 2012) dealt with magnetic Bragg scattering which is well localised in the reciprocal ($\vec{Q}$) space. However, a different situation arises when dealing with diffuse chiral scattering which spreads over the reciprocal space and may even overlap with other non-chiral contributions.

In the following, we discuss the effect of magnetic chirality on the cross section and polarization of the scattered beam and derive simple relations that compare with experiment, on the example of the archetypal system MnSi.

Finally we discuss the way chiral scattering affects the results of Neutron Spin Echo spectroscopy (NSE), both in the paramagnetic and the ferromagnetic neutron spin echo modes. For this purpose we introduce and compare the paramagnetic and the ferromagnetic Neutron Spin Echo methods, as the latter has not been discussed in the literature so far. At last, we discuss the insight provided by the vector nature of the (dipole) interaction between the neutron beam polarization and a magnetic sample on the Quantum Mechanical description of Larmor precession based methods.

2 Magnetic scattering of a polarized neutron beam

2.1 Cross section

The starting point is the Fourier transform of the long ranged dipole-dipole electromagnetic interaction potential between a neutron with magnetic moment $\vec{\sigma}$ scattered with a momentum transfer given by the scattering vector $\vec{Q}$ by electrons with spin $\vec{s}_i$, momentum $\vec{p}_i$ and at respective positions $\vec{r}_i$:

$$\begin{aligned} U_M(\vec{Q}) &= -\gamma\,\rho_0\,\vec{\sigma}\cdot\left[2\,\mu_B\sum_i\left[\hat{Q}\times(\vec{s}_i\times\hat{Q})-\frac{i}{Q}(\hat{Q}\times\vec{p}_i)\right]exp(i\vec{Q}\cdot\vec{r}_i)\right] \\ &= -\gamma\,\rho_0\,\vec{\sigma}\cdot\vec{M}_\perp \end{aligned} \tag{1}$$

with $\gamma = 1.91$, μ_B the Bohr magneton and $\rho_0 = \mu_0\,\mu_n$, where μ_0 is the vacuum permeability and μ_n the nuclear magneton. The magnetic interaction vector $\vec{M}_\perp$ is the projection perpendicular to $\vec{Q}$ of the Fourier transform of the magnetic moments distribution, both spin and orbital, created by the unpaired electrons of the scatterer. This relation is at the origin of the vector properties of magnetic neutron scattering, which are nowadays explained in textbooks and widely used to discriminate the magnetic from nuclear scattering contributions.

The implications for chiral magnetism were first discussed by Overhauser (1962) and Izyumov (1962) and led to the complete formalism developed almost simultaneously by Blume (1963) and Maleyev (1962). Following Blume, in the most general case, the magnetic scattering neutron cross section can be written as:

$$S_M(\vec{Q},\omega) = (\gamma\rho_o)^2 \frac{k_f}{k_i}\delta(E_f - E_i + h\omega)\cdot \sum_{q_i,q_f} p_{q_i}\Big[\langle q_i|\vec{M}_\perp^*|q_f\rangle\cdot\langle q_f|\vec{M}_\perp|q_i\rangle + i\,\vec{P}_i\cdot\Big(\langle q_i|\vec{M}_\perp^*|q_f\rangle \times \langle q_f|\vec{M}_\perp|q_i\rangle\Big)\Big], \tag{2}$$

where the subscripts i and f indicate the initial (before scattering) and final (after scattering) states, k and E label the momentum and energy of the neutron respectively, $h\omega$ is the energy transfer, $\vec{P}_i$ the polarization of the incoming beam and the quantum numbers q label the states of the scatterer which occupies an initial state q_i with a probability p_{q_i}.

The first term in the sum of Eq. (2) is the magnetic scattering cross section for an unpolarized neutron beam, S_M°, which is independent of the chiral magnetic properties of the scatterer:

$$S_M^\circ(\vec{Q},\omega) = (\gamma\rho_0)^2\frac{k_f}{k_i}\cdot\delta(E_f - E_i + h\omega)\cdot\sum_{q_i,q_f} p_{q_i}\Big[\langle q_i|\vec{M}_\perp^*|q_f\rangle\cdot\langle q_f|\vec{M}_\perp|q_i\rangle\Big]. \tag{3}$$

The second term in the sum of Eq. (2) is non-zero only if a polarized neutron beam interacts with chiral magnetic correlations, and is the dot product between $\vec{P}_i$ and a quantity that we will call the chiral scattering vector:

$$\vec{H}(\vec{Q},\omega) = (\gamma\rho_0)^2\frac{k_f}{k_i}\cdot\delta(E_f - E_i + h\omega)\cdot i\sum_{q_i,q_f} p_{q_i}\Big[\langle q_i|\vec{M}_\perp^*|q_f\rangle \times \langle q_f|\vec{M}_\perp|q_i\rangle\Big]. \tag{4}$$

Thus, $\vec{H}(\vec{Q},\omega)$ is collinear with $\hat{Q}$, antiparallel for a right handed and parallel for a left handed chirality, and its modulus can take any value between 0 and $S_M^\circ(\vec{Q},\omega)$ depending on the degree of chirality of the probed magnetic correlations. Consequently, we introduce two parameters: ζ for the handedness of the chiral magnetic correlations, with $\zeta = -1$ for right and $\zeta = +1$ for left, and η for the degree of chirality, or chiral fraction, defined as:

$$\eta(\vec{Q},\omega) = \frac{|\vec{H}(\vec{Q},\omega)|}{S_M^\circ(\vec{Q},\omega)}. \tag{5}$$

Therefore, $0 \le \eta \le 1$ with $\eta = 0$ for non-chiral and $\eta = 1$ for completely chiral magnetic correlations as it is the case e.g. for MnSi at low temperatures

(Grigoriev, 2005; Pappas et al., 2009; Kindervater et al., 2014). Hence, without any loss of generality the chiral scattering vector can be written as:

$$\vec{H}(\vec{Q}, \omega) = \eta\, \zeta\, S_M^{\circ}(\vec{Q}, \omega)\, \hat{Q}, \tag{6}$$

and the general relation for the cross section of Eq. (2) reduces to the simple generic form (Pappas et al., 2009):

$$S_M(\vec{Q}, \omega) = S_M^{\circ}(\vec{Q}, \omega)(1 + \eta\, \zeta\, \vec{P}_i \cdot \hat{Q}). \tag{7}$$

This equation highlights the vector properties of the interaction between a polarized neutron beam and chiral magnetic correlations, which also affects the cross section and as shown below for the extreme case, where $\eta = 1$ and $\vec{P}_i = \pm\hat{Q}$, the cross section may be either doubled, with respect to the unpolarized case, or completely vanish. In other words, depending on the direction of $\vec{P}_i$ there can be constructive or destructive interference between the nonchiral and chiral scattering, an effect observed in several systems including MnSi (Roessli et al., 2002; Grigoriev et al., 2005; Pappas et al., 2009; Grigoriev et al., 2013; Moskvin et al., 2013; Bannenberg et al., 2017; Pappas et al., 2011; Pappas et al., 2021):

$$S_M(\vec{Q}, \omega) = 2 \cdot S_M^{\circ}(\vec{Q}, \omega) \text{ for } \vec{P}_i = \zeta\, \hat{Q} \text{ and } \eta = 1,$$
$$S_M(\vec{Q}, \omega) = 0 \text{ for } \vec{P}_i = -\zeta\, \hat{Q} \text{ and } \eta = 1.$$

2.2 Polarization

Following the formalism of Blume the polarization of the scattered neutron beam, $\vec{P}_f$, is given by:

$$\begin{aligned}\vec{P}_f \cdot S_M(\vec{Q}, \omega) = (\gamma\rho_o)^2 \frac{k_f}{k_i} \delta(E_f - E_i + \hbar\omega) \cdot \sum_{q_i, q_f} \Big[& p_{q_i} \langle q_i | \vec{M}_{\perp}^{*} | q_f \rangle \cdot \langle q_f | \vec{P}_i \cdot \vec{M}_{\perp} | q_i \rangle \\ & + \langle q_i | \vec{P}_i \cdot \vec{M}_{\perp}^{*} | q_f \rangle \cdot \langle q_f | \vec{M}_{\perp} | q_i \rangle - \vec{P}_i \langle q_i | \vec{M}_{\perp}^{*} | q_f \rangle \cdot \langle q_f | \vec{M}_{\perp} | q_i \rangle \\ & - i \Big(\langle q_i | \vec{M}_{\perp}^{*} | q_f \rangle \times \langle q_f | \vec{M}_{\perp} | q_i \rangle \Big) \Big].\end{aligned} \tag{8}$$

The first three terms of the sum describe the general interaction between a neutron beam and magnetic correlations as derived by Halpern and Johnson (1939). This formalism shows that in the absence of chiral magnetic scattering the incoming beam polarization rotates or precesses by π around $\vec{M}_{\perp}$. The last term is specific to chiral magnetism and creates a polarization along $\vec{Q}$. The repercussions of this term are most clearly seen if the incoming beam is

depolarized, in which case, the scattered beam is polarized along the chiral scattering vector:

$$\text{for } \vec{P}_i = 0 \Rightarrow \vec{P}_f \cdot S_m^\circ(\vec{Q}, \omega) = -\vec{H}(\vec{Q}, \omega). \tag{9}$$

And by using Eq. (6):

$$\text{for } \vec{P}_i = 0 \Rightarrow \vec{P}_f = -\eta\, \zeta\, \hat{Q}. \tag{10}$$

This result is always valid independently from e.g. the existence of a quantisation axis defined by a magnetic field. This is a striking difference from usual neutron polarizers, ferromagnetic single crystals or magnetic multilayers, which create a polarization collinear to the quantisation axis defined by a magnetic field.

In the most general case, for a well defined direction of $\vec{M}_\perp$, induced e.g. by magnetocrystalline anisotropy, the scattered beam polarization is given by Brown (2001) and Lelièvre-Berna (2024):

$$\begin{aligned} \vec{P}_f &= \frac{S_M^\circ(\vec{Q}, \omega)}{S_M(\vec{Q}, \omega)} \begin{bmatrix} -(P_{i,x} + \eta\, \zeta) \\ P_{i,y}(2\, m_y^2 - 1) + 2P_{i,z}\, \Re(m_y m_z^*) \\ P_{i,z}(2\, m_z^2 - 1) + 2P_{i,y}\, \Re(m_z m_y^*) \end{bmatrix} \\ &= \frac{1}{1 + \eta\, \zeta\, P_{i,x}} \begin{bmatrix} -(P_{i,x} + \eta\, \zeta) \\ P_{i,y}(2\, m_y^2 - 1) + 2P_{i,z}\, \Re(m_y m_z^*) \\ P_{i,z}(2\, m_z^2 - 1) + 2P_{i,y}\, \Re(m_z m_y^*) \end{bmatrix} \end{aligned} \tag{11}$$

with $P_{i,\alpha}$ the x, y, z components of the incoming beam polarization, $m_\alpha = M_\alpha / M_\perp$, the normalised components along y, z of the Fourier transform of the magnetic moments distribution perpendicular to $\vec{Q}$, $m_\alpha^2 = m_\alpha m_\alpha^*$ and the symbol $\Re$ standing for the real part of a complex quantity. The normalisation by the cross sections has been overlooked in the literature so far and is a direct consequence of Eq. (8) ensuring that the modulus of $\vec{P}_f$ does not exceed 1. For comprehensive simulations the reader is referred to Lelièvre-Berna (2024).

As mentioned above, if the direction of $\vec{M}_\perp$ is well defined, the non-chiral term leads to a π rotation of the polarization vector around $\vec{M}_\perp$. In this case the modulus of the polarization does not change and $|\vec{P}_f| = |\vec{P}_i|$. A different situation occurs when the magnetic moments are homogeneously distributed in the plane perpendicular to $\vec{Q}$, as e.g. for Heisenberg magnets or helices. In this case the direction of $\vec{M}_\perp$ is not well defined and the scattering results from all possible directions of $\vec{M}_\perp$. Consequently, the polarization of the scattered neutron beam simplifies to:

$$\vec{P}_f = -\hat{Q}\,[\vec{P}_i \cdot \hat{Q} + \eta\, \zeta]/[1 + \eta\, \zeta\, \vec{P}_i \cdot \hat{Q}]. \tag{12}$$

Thus, in the absence of chirality, only the component of $\vec{P}_i$ along $\vec{Q}$ is preserved, although flipped. In this case the modulus of the final polarization can be reduced and in the extreme case where $\vec{P}_i \perp \vec{Q}$ the scattered beam is completely depolarized with $|\vec{P}_f| = 0$.

Experimentally it is impossible to distinguish between a rotation of the polarization vector and a loss of polarization as long as a magnetic field is applied at the sample, in which case only the projection of the beam polarization along this magnetic field can be measured. The way out is a zero magnetic field polarimeter such as e.g. Cryopad (Tasset, 1989; Lelièvre-Berna, 2005, 2007) or MuPad (Janoschek et al., 2007), consisting of a zero magnetic field area around the sample and modules that allow to control the direction of $\vec{P}_i$ and $\vec{P}_f$, thus providing full information on both the direction and modulus of $\vec{P}_f$.

3 The case of MnSi

In his original publication, Blume (1963) illustrated the non-trivial interplay between polarized neutron beams and chiral magnetism using the most simple example of a magnetic helix. This structure is the ground state at zero magnetic field of the skyrmion hosting system MnSi, and other systems of the B20 family, where single magnetic chirality results from the handedness of the crystal structure (Dyadkin et al., 2011). The effect of magnetic chirality, left handed in the case of MnSi, was first seen on the scattering of polarized neutrons at the helical satellites around structural Bragg peaks (Roessli, 2002) and soon after by polarized small angle neutron scattering (SANS) (Grigoriev, 2005).

The left handed helical arrangement, as it is the case in MnSi, of the spin unit vector $\hat{s}$ in the $\hat{y}-\hat{z}$ plane propagating along $\hat{x}$, is given by:

$$\begin{aligned} \hat{s}\,(\vec{x}) &= \hat{y}\ cos\,(2\pi\hat{x}\cdot\vec{r}/\ell) - \hat{z}\ sin\,(2\pi\hat{x}\cdot\vec{r}/\ell) = \\ &= \tfrac{1}{2}[(\hat{y} + i\,\hat{z})\,e^{i2\pi\hat{x}\cdot\vec{r}/\ell} + (\hat{y} - i\,\hat{z})\,e^{-i2\pi\hat{x}\cdot\vec{r}/\ell}], \end{aligned} \tag{13}$$

with ℓ the pitch of the helix. The perfect helix is thus a special case with the real and imaginary parts of $\vec{M}_\perp$ being equal to each other and leading to the utmost manifestation of magnetic chirality in polarized neutron scattering.

We will in the following focus on the SANS geometry schematically shown in Fig. 1 and note that these considerations also apply around any other equivalent Bragg peak. We chose a coordinate system such that $\hat{x}$ is parallel to $\vec{Q}$, $\hat{y}$ points along the neutron beam propagation vector $\vec{k}_i$ and $\hat{z}$ complements the cartesian coordinate system. This implies that the coordinate system varies with $\vec{Q}$ and thus it is not the same when neutrons are scattered to the right or left of the neutron beam.

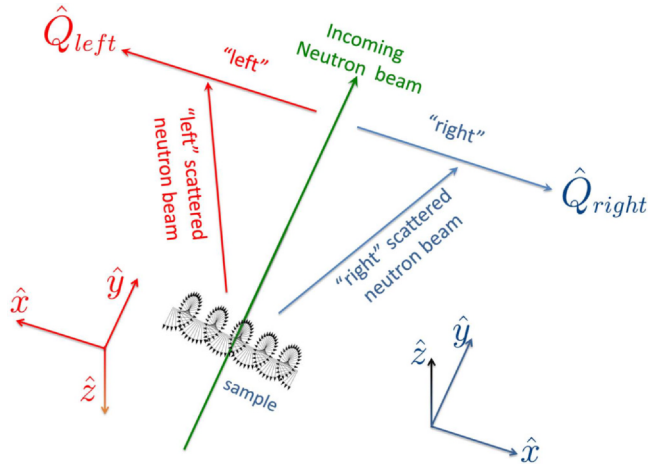

FIG. 1 Geometry for the magnetic small angle neutron scattering by helices propagating along $\hat{x}$, which is collinear with $\vec{Q}$. The other coordinates are chosen such that $\hat{y} \| \vec{k}_i$, the neutron beam propagation vector, and $\hat{z}$ complements the cartesian system. As the coordinate system varies with $\vec{Q}$ it is not the same when neutrons are scattered to the right and left of the neutron beam.

In the SANS geometry considered here, the coordinate systems of all possible reflections share the same $\hat{y}$ but rotate around this axis following the scattering vector while $\vec{Q} = 0$ is a singular point.

3.1 Ordered helical phase

The resulting scattering pattern from an unpolarized neutron beam is illustrated by Fig. 2A and has two satellite peaks at $\vec{Q} = \vec{\tau} = \pm\tau\,\hat{x}$, with $\tau = 2\pi/\ell$, i.e. left and right respectively of $Q = 0$, or any other equivalent Bragg peak. If the beam is polarized, the effect of magnetic chirality becomes visible and as a consequence of Eq. (7) the peak for which $\hat{Q}\cdot(\zeta\ \vec{P}_i) = 1$ is enhanced whereas the one for $\hat{Q}\cdot(\zeta\ \vec{P}_i) = -1$ is extinct, as shown in Fig. 2B and C respectively.

In the presence of a ferromagnetic component, e.g. induced by an external magnetic field in the so-called conical phase of chiral magnets, the spin unit vector is given by:

$$\hat{s}\,(\vec{r}) = \hat{x}\ cos\,(\phi) + sin\,(\phi)(\hat{y}\ cos\,(2\pi\hat{x}\cdot\vec{r}/\ell) - \hat{z}\ sin\,(2\pi\hat{x}\cdot\vec{r}/\ell)) \qquad (14)$$

with ϕ the angle between the magnetic moments and the propagation vector of the helix as illustrated in Fig. 2. In this case chiral satellites coexist with a non-chiral ferromagnetic peak at $Q = 0$. Of course, as neutrons "see" only the components of the spin perpendicular to the scattering vector $\vec{Q}$, in the geometry considered here this ferromagnetic component would have been invisible and the scattering patterns would have been the same as in Fig. 2A and B.

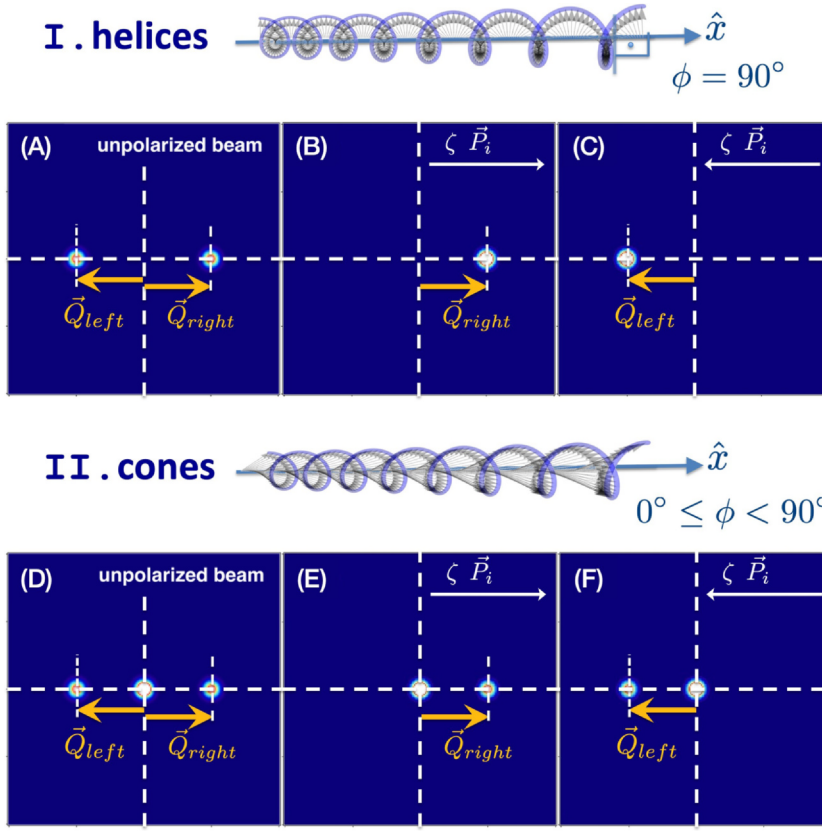

FIG. 2 Small angle neutron scattering patterns originating from a chiral helical (A–C) and a conical structure (D–F). In both cases, the helical component, perpendicular to the helix propagation vector along $\hat{x}$, leads to chiral Bragg peaks – satellites – around the position $Q = 0$. The interaction with a polarized neutron beam leads, according to Eq. (7), to the patterns B–C and D–E. The existence of a ferromagnetic component leads to a non-chiral ferromagnetic Bragg peak at $Q = 0$, the intensity of which is independent from the polarization of the incoming beam as illustrated by the patterns (D–F).

However, in the presence of several equivalent crystallographic directions, as e.g. in the tilted spiral phase of Cu_2OSeO_3 (Qian et al., 2018; Chacon et al., 2018), the scattering patterns should include a ferromagnetic peak as shown in Fig. 2D–F with a weight given from the specific magnetic structure and the angle ϕ.

3.2 Paramagnetic phase

In the case of MnSi, just above T_C the helical Bragg (satellite) peaks are replaced by a broad diffuse scattering, which concentrates on the sphere with

radius $\tau = 2\pi/\ell$, as shown in Fig. 3A (Grigoriev, 2005; Pappas et al., 2009, 2011; Hamann, 2011; Janoschek, 2013b). At higher temperatures, this diffuse scattering broadens and its centre moves towards $Q = 0$ (Ishikawa, 1985; Hamann, 2011).

In the following, for the sake of simplicity and without any loss of generality, we adopt the Ornsten-Zernicke formalism and describe this diffuse scattering by simple Lorentzian functions centred at $Q = \tau$ for the chiral and at $Q = 0$ for a non-chiral ferromagnetic component.

The pattern of Fig. 3A implies that all local helical propagation vectors are homogeneously distributed in space and only the correlation length along the direction of the helix is important. In the absence of any non-chiral (e.g. ferromagnetic) contribution the cross section for an unpolarized neutron beam becomes:

$$S_M^{\circ}(\vec{Q}) \propto \frac{C}{(Q-\tau)^2+\kappa^2} + \frac{C}{(Q+\tau)^2+\kappa^2} = 2C\,\frac{Q^2+\tau^2+\kappa^2}{(Q^2-\tau^2)^2+2\kappa^2(Q^2+\tau^2)+\kappa^4}, \tag{15}$$

where C is a quantity reflecting the physics of the scattering process (including the magnetic form factor) and $\kappa = 2\pi/\xi$ with ξ the characteristic correlation length. We note that Eq. (15) is a simplified version of Eq. (7) in Grigoriev (2005).

The resulting scattering patterns for unpolarized and polarized neutron beams are given in Fig. 3A–C with the corresponding Q-dependent intensities depicted in Fig. 3D–F. Consequently, the scattering is fully chiral despite the finite correlation length.

At high temperatures, however, ξ becomes significantly shorter than the helical pitch in which case a crossover to non-chiral (e.g. ferromagnetic) correlations may occur as observed e.g. in MnSi (Ishikawa, 1985; Hamann, 2011). Consequently over an intermediate region the scattering would be a superposition of chiral scattering centred at $Q = \tau$ and a non-chiral scattering centred at e.g. $Q = 0$:

$$S_M^{\circ}(\vec{Q}) \propto \frac{C\cos^2(\phi)}{Q^2+\kappa^2} + \frac{2C\sin^2(\phi)(Q^2+\tau^2+\kappa^2)}{(Q^2-\tau^2)^2+2\kappa^2(Q^2+\tau^2)+\kappa^4} \tag{16}$$

where ϕ is the average angle between the magnetic moments and the local helix propagation vectors, defined as in Fig. 2.

Following Eq. (7), the interaction with a polarized neutron beam leads to the scattering patterns of Fig. 4C–F. Figs. 3 and 4 illustrate the simplest way to determine experimentally the magnetic vector chirality: by measuring the intensity of a scattered polarized neutron beam, while reversing the incoming

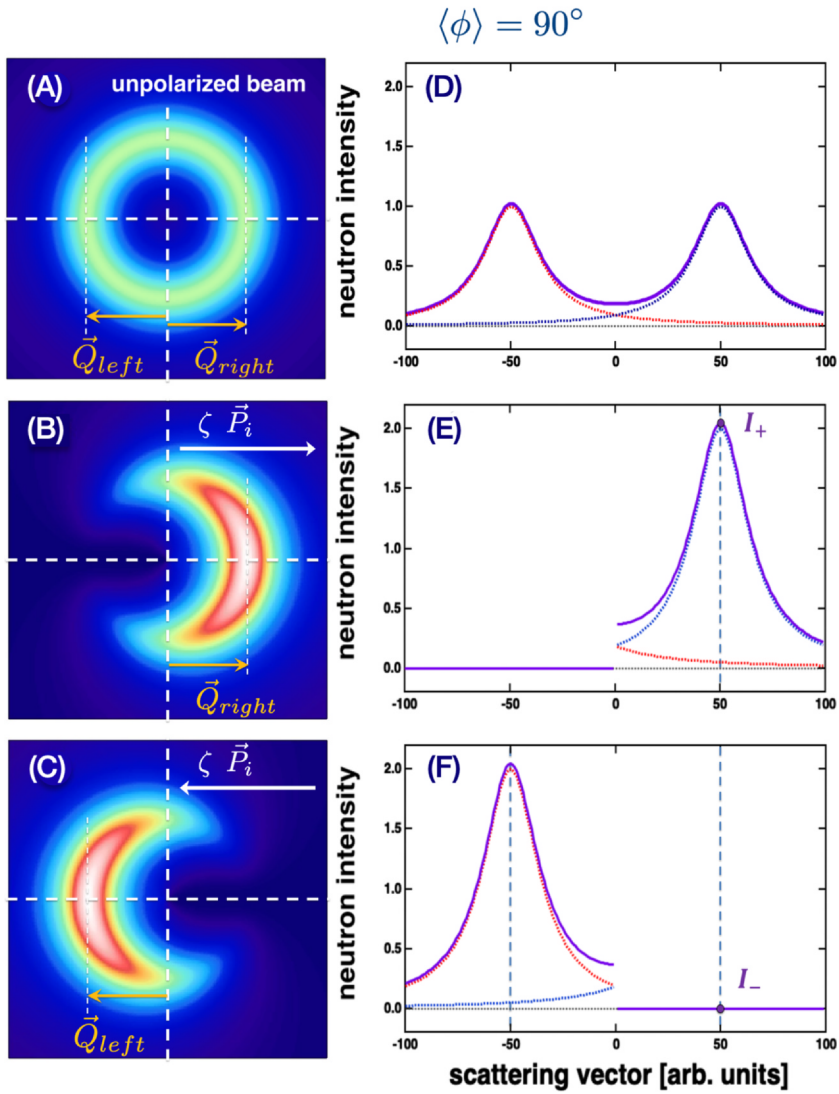

FIG. 3 Small angle neutron scattering patterns originating from chiral correlations (A–C), i.e. with an average angle between the spins and the helical vector $\langle\phi\rangle = 90°$. The helical component (blue and red dotted curves in D–F for the right and left satellites respectively), perpendicular to the helix propagation vector along $\hat{x}$, leads to chiral scattering around $Q = \tau$, which for a polarized neutron beam is direction-dependent (left/right). The patterns are derived from Eq. 17 assuming $\kappa = 2\tau$.

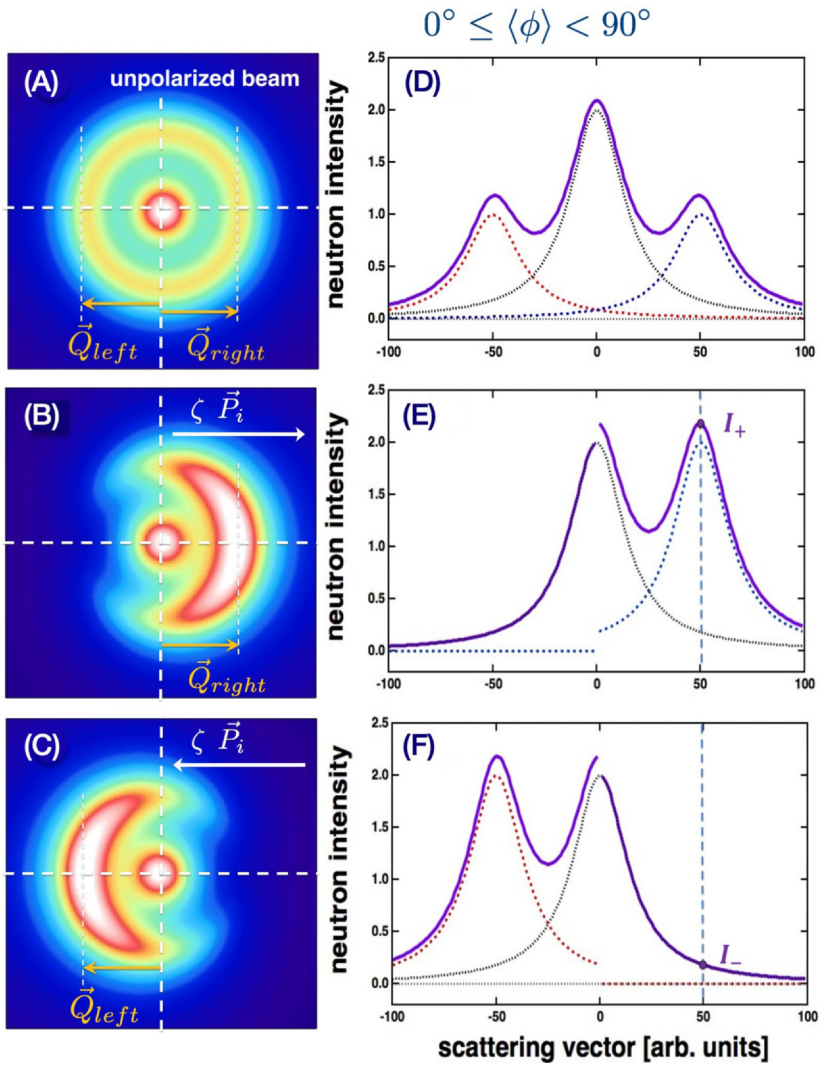

FIG. 4 Small angle neutron scattering patterns originating from chiral conical correlations, i.e. with an average angle between the spins and the helical vector $\langle\phi\rangle < 90°$ (A-C). The helical component (blue and red dotted curves for the right and left satellites respectively in D-F), perpendicular to the helix propagation vector along $\hat{x}$, leads to chiral scattering around $Q = \tau$ as before, and is superimposed on the non-chiral ferromagnetic scattering (black dotted curve) centred at $Q = 0$. The patterns are derived from Eq. 17 assuming $\kappa = 2\tau$ and $\langle\phi\rangle < 45°$.

neutron beam polarization, which should be parallel/antiparallel to the scattering vector $\vec{Q}$. Indeed in this case:

$$\text{for } \vec{P_i} = -\zeta\, \hat{Q} \quad S_M(\vec{Q}) \propto \frac{C\cos^2(\phi)}{Q^2+\kappa^2} + \sin^2(\phi)\left[\frac{C}{(Q-\tau)^2+\kappa^2} + \frac{C}{(Q+\tau)^2+\kappa^2}\right] \quad (17)$$

$$\text{and for } \vec{P_i} = \zeta\, \hat{Q} \quad S_M(\vec{Q}) \propto \frac{C\cos^2(\phi)}{Q^2+\kappa^2}.$$

If the intensities at e.g. $Q=\tau$ are designated as I_+ and I_- respectively, as shown in Figs. 3 and 4, following Eq. (7) the chiral fraction is given by the ratio:

$$\eta = \eta(Q=\tau) = \frac{I_+ - I_-}{I_+ + I_-} \quad (18)$$

where $\eta = 1$ for $\langle\phi\rangle = 90°$, the case illustrated in Fig. 3, while $\eta = 0.848$ for $\langle\phi\rangle = 45°$ and $\xi = \ell/2$, thus $\kappa = 2\tau$, the situation of Fig. 4.

At $Q=\tau$ Eq. (17) leads to:

$$\sin^2(\phi) = \left[1 + \frac{1-\eta}{\eta}\frac{[2+(\kappa/\tau)^2]\,[1+(\kappa/\tau)^2]}{(\kappa/\tau)^2\,[4+(\kappa/\tau)^2]}\right]^{-1}. \quad (19)$$

Thus, in this case, the magnetic chirality probed by polarized neutrons reflects the topology of magnetic correlations and provides a direct measurement of the average angle between the magnetic moments and the (local) helical propagation vectors. In the following section we discuss the consequences in the specific case of MnSi.

Eq. (17) shows that there is no simple relation between the correlation length and the chiral fraction η. The simple relation between κ and η suggested in Grigoriev (2005) is inconsistent with the Blume (1963) and Maleyev (1962) formalism (and Eqs. (17) and (18)), which explains the disagreement between the predicted values and our experimental data shown here and in Pappas et al. (2009, 2011).

Finally, we would like to point out that the case of MnSi and other systems of the same family (e.g. Bannenberg et al., 2017; Dyadkin et al., 2011; Grigoriev et al., 2013; Moskvin et al., 2013; Pappas et al., 2021) and beyond (e.g. Marty et al., 2008; Dally et al., 2020), is special in that they are characterised by single magnetic chirality induced by the chiral structure of the lattice. When this is not the case, a reduction of η at the helical satellite position may reflect the coexistence of domains with opposite chirality as e.g. in mutliferroics, where an imbalance between domains with opposite chirality can be induced and controlled by electric fields (Brown et al., 1998, 2002; Ishiwata et al., 2010; Hearmon et al., 2012; Yamasaki et al., 2007; Rodríguez-Velamazán et al., 2018; Baum, 2013; Holbein, 2016; Finger et al., 2010b; Hutanu et al., 2014).

3.3 Chiral fraction in the paramagnetic phase

Our very accurate measurements of chirality with spherical polarimetry (Pappas et al., 2009, 2011) revealed that the magnetic correlations of MnSi are chiral also in the paramagnetic phase reaching $\eta = 1$ within a limited temperature range between $T_C \sim 29$ K and $\sim T_C + 1$ K. This observation led to a debate on the nature of this highly correlated phase, that has strong characteristics of a spin-liquid-like phase with particular topology. Pursuing the analysis of the previous sections, we will in the following analyse existing data, complemented by additional measurements, using Eq. (19) and will deduce the evolution of the topology of magnetic correlations, while these build up above T_C.

The experiment reported in Ref. Pappas et al. (2009, 2011) was performed on the neutron spin echo spectrometer IN15 of the ILL, which has a polarized cold neutron beam, $\lambda \geq 0.7$ nm, and a highly efficient polarization analyser (efficiency $\sim$ 99%) in front of a $32 \times 32\,\mathrm{cm}^2$ position sensitive detector at a distance of 4.6 m from the sample. At a wavelength of $\lambda = 0.9$ nm used for these experiments, the detector covers only a fraction of the whole scattering pattern illustrated by the blue dotted rectangle of Fig. 5. For the chirality analysis $\vec{Q}$ must be well defined and for this reason the intensity was integrated over an area inside the red rectangle illustrated in Fig. 5.

For a reliable determination of η it is also crucial to obtain a good signal over background ratio and reach an accurate determination of the background. For these measurements, which were done with the sample in a shielded zero-magnetic-field chamber (thus minimising any spurious effects of the

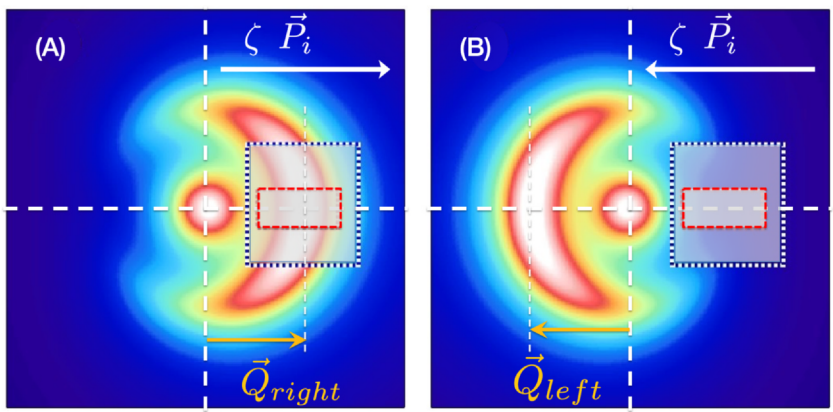

FIG. 5 Small angle neutron scattering patterns originating from chiral conical correlations, i.e. with an average angle between the spins and the helical vector $\langle\phi\rangle < 90^\circ$. The helical component, perpendicular to the helix propagation vector leads to chiral scattering around $Q = \tau$, reflected in the difference between the patterns of A and B. This is superimposed on the non-chiral ferromagnetic scattering centred at $Q = 0$. The angular coverage by the IN15 detector in the experiment discussed in the text is also indicated by the black rectangle whereas the red rectangle depicts the area over which the scattered intensity was integrated.

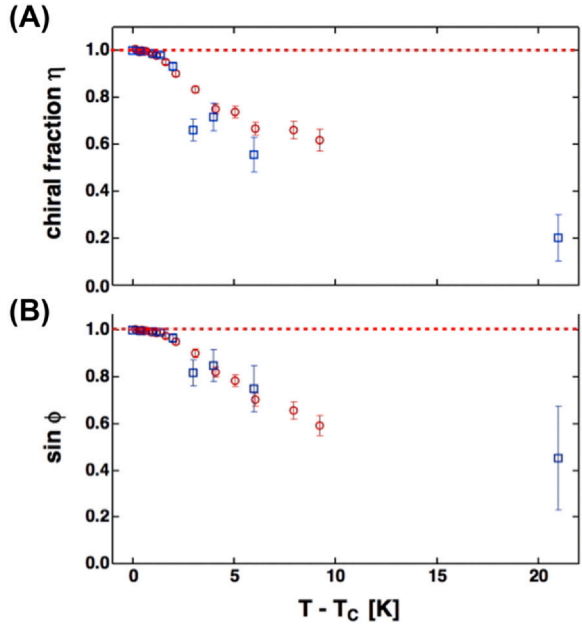

FIG. 6 Chiral fraction (A) of the left-handed helical/conical correlations and average angle ϕ (B) between the magnetic moments and the local helix propagation axis deduced using Eq. (19) in the case of MnSi.

demagnetisation field on the neutron beam polarization) the background was determined at high temperatures using neutron polarization analysis.

Figs. 6 and 7 depict (over the whole temperature range investigated and close to T_C respectively) an information on the topology of magnetic moments that is directly obtained by polarized neutron scattering. Chirality increases with decreasing temperature and saturates at $T_C + 1$ K where $\phi = 90^\circ$, i.e. at this highly correlated and chiral fluctuating phase above T_C the magnetic moments are locked in the plane perpendicular to the local helix propagation axes, which are homogeneously distributed in the space.

A surprising result is that helical correlations persist even at temperatures as high $\sim 2T_C$, where $\eta \sim 0.2$ leads to an average angle of $\phi \sim 25^\circ$. At this temperature however the correlation length does not exceed 0.7 nm (Hamann, 2011), which is only $\sim 4\%$ of the helical pitch, spanning only a couple of Mn atoms. This indicates that in MnSi, the Dzyaloshinskii-Moriya interaction is not just a perturbation that shows up only close to T_C as often assumed (e.g. Grigoriev, 2005, 2010; Janoschek et al., 2013a), but its influence on the magnetic correlations extends over an extremely wide temperature range. The robustness of these chiral correlations against thermal fluctuations is reminiscent of the behaviour of low dimensional magnets and could be related to the one-dimensional character of helices.

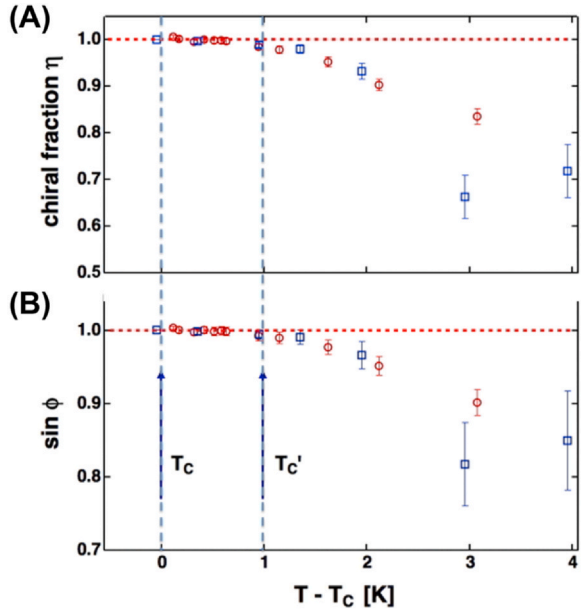

FIG. 7 Same data as in Fig. 6 for the chiral fraction (A) of the left-handed helical/conical correlations and the average angle ϕ (B) in the case of MnSi highlighting the behaviour close to T_C.

4 Neutron spin echo spectroscopy (NSE)

In Neutron Spin Echo spectroscopy (NSE) the Larmor precession of a neutron beam polarization in a magnetic field is used to directly measure the energy transfer at the sample. In this way the energy resolution is decoupled from other beam characteristics like monochromatisation and collimation and the highest resolution in energy transfer (of the order of some neV) can be reached while keeping the high intensity advantage of a beam, which is only 10–20% monochromatic. This method has been the subject of numerous books and reviews (see e.g. Mezei, 1980; Mezei et al., 2003) and for this reason we will refrain here from an extensive introduction but will focus on the interplay with chiral magnetic scattering. The starting point is the paramagnetic NSE and after a short mention of polarimetric NSE we will discuss the ferromagnetic NSE method, which has not been addressed in the literature so far. Finally, we discuss the insights that the vector nature of the (dipole) interaction between the polarization of the neutron beam and a magnetic sample provides for the quantum mechanical description of methods based on Larmor precession.

4.1 Paramagnetic NSE

NSE uses a polarized neutron beam, consequently polarization analysis is inherent to this method. As a general introduction to the terminology, the

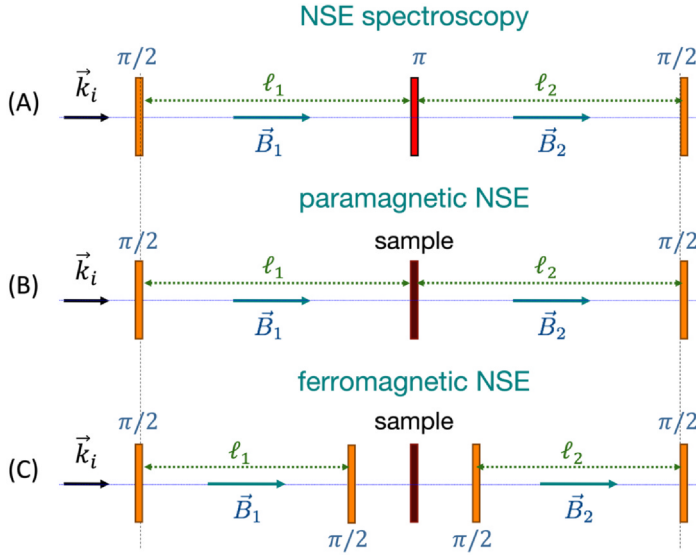

FIG. 8 Schematic representation of a Neutron Spin Echo setup, consisting of a sequence of 3 flips $\pi/2$-precessions-π at the sample position-precessions-$\pi/2$ (A), which is equivalent to the Hahn echo sequence in NMR. For the paramagnetic NSE, (B), the π flip, which marks the reversal point of Larmor precessions (before and after the scattering process), is realised by the (para) magnetic scattering of the sample. The ferromagnetic NSE shown in (C) consists of a sequence of four $\pi/2$ flips ($\pi/2$-precessions-$\pi/2$-sample area-$\pi/2$-precessions-$\pi/2$) and is equivalent to the stimulated echo sequence in NMR. The two $\pi/2$ flippers around the sample stop and resume precession labelling respectively and thus decouple the sample area from the NSE measurement. The echo condition for all cases requires the magnetic field integrals over the neutron beam trajectory in the precession areas to be equal, which in the simple case (constant magnetic field) considered here leads to $B_1\ell_1 = B_2\ell_2$.

classical neutron spin echo (NSE) setup consists of a sequence of 3 flips ($\pi/2$-precessions-π at the sample position-precessions-$\pi/2$) as schematically shown in Fig. 8A and is equivalent to the Hahn echo sequence in NMR. The echo condition requires the magnetic field integrals over the neutron beam trajectory before and after the π flip, $B_1\ell_1 = B_2\ell_2$, to be equal.

For the paramagnetic NSE the π flip, which marks the reversal point of Larmor precessions (before and after the scattering process), is realised by the (para) magnetic scattering of the sample as schematically shown in Fig. 8B and explained in Fig. 9, after Murani and Mezei (1980), and where as in Fig. 1, $\vec{Q}$ is along $\hat{x}$ and the neutron beam propagates along $\hat{y}$. The (precession) magnetic field $\vec{B}$ is applied along $\hat{y}$ and the precessions take place in the $x-z$ plane which also contains $\vec{Q}$, a condition for paramagnetic NSE.

At the sample position the finite wavelength spread of the beam leads to a distribution of precession angles, given that the precession angle is directly proportional to the wavelength, and thus the neutron beam appears to be depolarised.

Here we consider a subsection of the neutron beam with a well defined (delta function ideally) precession phase, such that the incoming polarization at the sample is well defined and equal to $\vec{P}_i$, which is in the precession $x-z$ plane. Assuming isotropic non-chiral scattering and following Eq. (12), the polarization of the scattered beam will be given by $\vec{P}_f = -\hat{Q}\cdot(\hat{Q}\cdot\vec{P}_i)$, which implies the component along $\vec{Q}\|\hat{x}$, will flip and $\vec{P}_{f,\|} = -\vec{P}_{i,\|}$. On the other hand, the component along $\hat{z}$, which is perpendicular to $\vec{Q}$, will become depolarized by the scattering process and $\vec{P}_{f,\perp} = 0 = \vec{P}_{i,\perp}/2 - \vec{P}_{i,\perp}/2$.

Consequently the components of the scattered polarization along $\hat{x}$ and $\hat{z}$ can be recombined to give two vectors of equal magnitude, $\vec{P}_{NSE} = -(\vec{P}_{i,\|} - \vec{P}_{i,\perp})/2$ and $\vec{P}_{depol} = -(\vec{P}_{i,\|} + \vec{P}_{i,\perp})/2 = -\vec{P}_i/2$ with $\vec{P}_{i,\|} = \hat{x}\cdot(\vec{P}_i\cdot\hat{x})$ and $\vec{P}_{i,\perp} = \hat{z}\cdot(\vec{P}_i\cdot\hat{z})$.

With respect to $\vec{P}_i$, $\vec{P}_{NSE}$ has undergone a precession of π around $\hat{z}$. Through this precession the z-axis becomes a mirror symmetry axis, where the order of the phases is mirrored/reversed (those in front go behind), as required for the echo condition. On the other hand $\vec{P}_{depol}$ has only undergone a 180° phase shift with respect to $\vec{P}_i$ and this component will keep precessing and will be depolarized at the last $\pi/2$ flipper. In this way it is possible to explain why magnetic scattering plays the role of a π flipper in NSE, under the condition that $\vec{Q}$ is in the precession plane, and why only half of the magnetic cross section gives an echo. The other half is depolarized and half of it (thus 1/4 of the magnetic cross section) is transmitted by the polarization analyser in front of the detector and contributes to the background of the NSE measurement.

If the magnetic moments are not homogeneously distributed in the $y-z$ plane but point along $\hat{z}$ following Fig. 9 the totality of the magnetic cross section will lead to an echo. On the other hand, if the magnetic moments are along $\hat{y}$ the final result will be a 180° phase shift for the totality of the magnetic scattering. In this case an additional π flipper is needed which implies that the paramagnetic NSE method fails and there is no discrimination of the magnetic scattering from other contributions. In the case of a homogeneous distribution of the magnetic moments, the result is a mixture of these two extreme cases, with 50% of the cross section giving an echo and 50% a 180° phase shift, as discussed above. However, in this case it is not possible to distinguish between $M_{\perp,y}$ and $M_{\perp,z}$ because the spin flip of the polarization component along $\hat{x}$ results from all components of $\vec{M}_\perp$.

The paramagnetic NSE method is very powerful because it leads to an unambiguous discrimination of magnetic dynamics from all other contributions. As (para) magnetic scattering acts as a π flipper an echo obtained without the π-flipper at the sample is the fingerprint of magnetic scattering. The drawback of this straightforward distinction between magnetic and non-magnetic scattering comes with the cost of a reduced by 2 echo amplitude and increased background. The advantage is enormous as this method allows for measuring weak magnetic signals even on top of an intense (but not modulated) background.

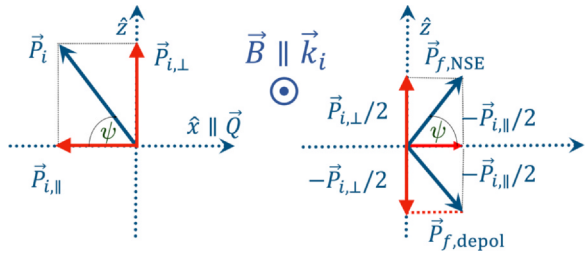

FIG. 9 Schematic drawing of the change of the beam polarization due to the (para)magnetic scattering at the sample, on the example of one subsection with a well defined (delta function ideally) precession phase. Due to the paramagnetic scattering the component of the incoming beam polarization which is along the scattering vector $\vec{Q}$ undergoes a spin flip, whereas the component perpendicular to it depolarizes. As a result, in average, half of the signal precesses by π around the axis perpendicular to $\vec{Q}$ and leads to an echo, without the need of any additional π flipper, whereas the other half undergoes a phase shift of 180° and contributes to the depolarized background.

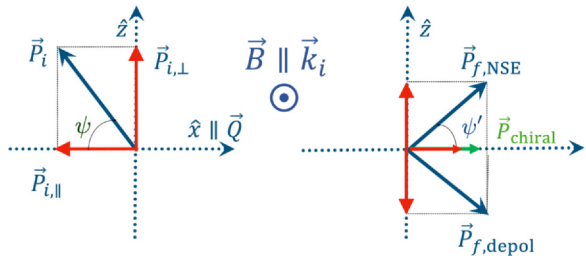

FIG. 10 Similar drawing as in Fig. 9 highlighting the effect of chiral scattering on paramagnetic NSE. The polarization along $\vec{Q}$ created by the chiral correlations affects the final result by introducing a phase shift, seen in the difference of the angles ψ and ψ'.

These considerations hold also in the presence of chiral scattering. In this case, the scattered beam polarization is given by Eq. (12) and results from the normalised sum of the non-chiral $-\hat{Q}\cdot(\hat{Q}\cdot\vec{P}_i)$ and chiral $-\hat{Q}\,\eta\,\zeta$ terms. As mentioned above, the latter creates a polarization, which however is not along $\vec{B}$ but along $\hat{Q}$. It is thus in the precession plane and contributes to NSE. As schematically shown in Fig. 10 also the combination of these two terms generates a π flip, leading to echo condition, but with a phase shift in comparison to the non-chiral case (seen in the difference of the angles ψ and ψ'). Averaged over all possible orientations of $\vec{P}_i$ this shift leads to a reduced echo amplitude by a factor that is a function of η and the scattering geometry. On the other hand, the chiral polarization leads to an overall echo phase shift with respect to a reference (e.g. equatorial plane) when measuring diffuse scattering with a position sensitive detector as shown in Fig. 5.

Thus the paramagnetic NSE method accesses the combined dynamics of both the chiral and non-chiral cross sections. These two terms can be disentangled by the polarimetric NSE method, which combines NSE with a zero

magnetic field polarimeter around the sample (e.g. Cryopad Tasset, 1989; Lelièvre-Berna, 2005, 2007) and has been described in detail in Pappas et al. (2008, 2009) and Lelièvre-Berna et al. (2009). This method has been applied to MnSi, where within the experimental accuracy, the same dynamics has been found for the chiral and non-chiral scattering (Pappas et al., 2009, 2011). This in retrospect is not surprising given the single chirality and simple helical correlations of this system. There is however no reason that this should always be the case and different dynamics for the two cross sections could be found in more complex magnets than MnSi.

4.2 Ferromagnetic NSE

In the following we focus on ferromagnetic NSE, which consists of a sequence of four $\pi/2$ flips ($\pi/2$-precessions-$\pi/2$-sample area-$\pi/2$-precessions-$\pi/2$) schematically shown in Fig. 8C and is equivalent to the stimulated echo sequence in NMR. The two $\pi/2$ flippers around the sample stop and resume precession labelling respectively and thus decouple the sample area from the NSE measurement. In this way it is possible to either incorporate additional elements in the setup including re-polarizers, as required for the intensity modulated (Farago and Mezei, 1986) and polarimetric NSE (Pappas et al., 2008, 2009; Lelièvre-Berna et al., 2009), or apply high magnetic fields at the sample independently of the precession field, as in the case of ferromagnetic NSE.

Similarly to the paramagnetic NSE, also the four $\pi/2$ sequence leads to an echo for only half of the scattering cross section whereas the other half is depolarized and is seen as background. In the following we look more closely into the ferromagnetic NSE and also explain why the echo persists and with the same amplitude independently of whether the two $\pi/2$ flips around the sample add to a π flip or subtract, which would correspond to no flip at all (Ross Stewart).

The principle of ferromagnetic NSE has not been discussed in the literature so far, and for this reason we start by considering the simple case of coherent nuclear scattering (A in Fig. 11) before moving to the non-chiral and chiral magnetic scattering (B and C respectively in Fig. 11).

We use again the same cartesian system of coordinates as above (see also Fig. 1), where $\hat{y}$ is along the beam propagation vector and $\hat{x}$ perpendicular to it and along $\vec{Q}$. We will further assume that a (strong) magnetic field is applied along $\vec{Q}$ and will consider the scattering geometry in the $x-y$ plane at four characteristic points of the setup as shown in Fig. 11: (I) just after the 2nd $\pi/2$ flip, which stops the precession labelling required for NSE, (II) and (III) just before and after scattering at the sample respectively and finally (IV) just before the 3rd $\pi/2$ flip, which resumes precession labelling. We further assume that the $\pi/2$ flips at I and IV subtract, which highlights the π flip generated by the ferromagnetic NSE. Nevertheless, our approach is also valid when these two $\pi/2$ flips add to a π flip, in which case the components $\vec{P}_{f,\mathrm{NSE}}$ and $\vec{P}_{f,\mathrm{depol}}$ are simply swapped.

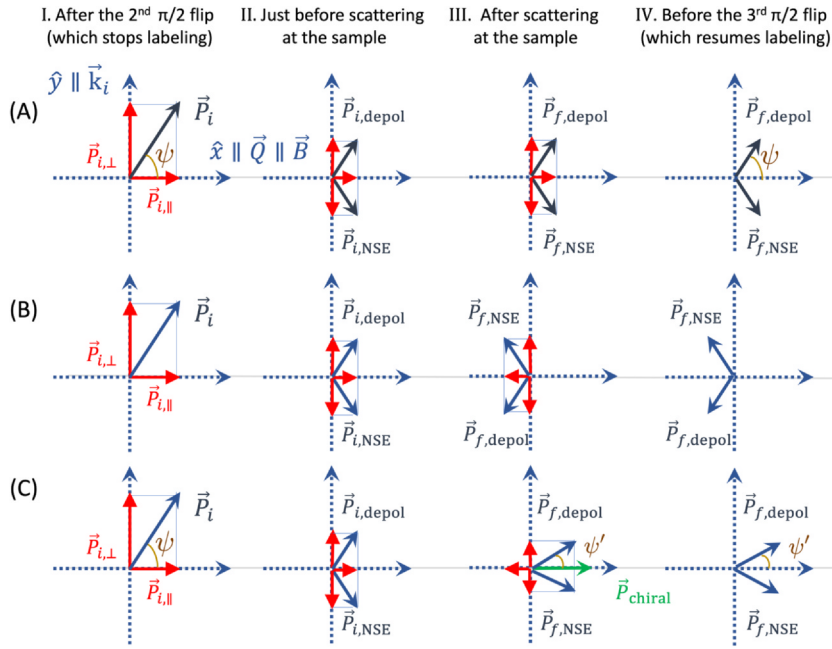

FIG. 11 Schematic drawings, similar to those of Figs. 9 and 10, of the evolution of the beam polarization (on the example of one subsection with a well defined – delta function ideally – precession phase) for the ferromagnetic NSE, in the case of (A) nuclear coherent, (B) paramagnetic and (C) chiral magnetic scattering (see text).

Before the sample, i.e. at the points I and II, the configuration is the same for all three cases considered here. The $\pi/2$ flip at the point I brings the polarization components, which were previously distributed in the $x-z$ precession plane, as in the paramagnetic NSE case and shown in Figs. 9 and 10, into the $x-y$ plane. Here we consider again a subsection of the neutron beam with a well defined (delta function ideally) precession phase, such that the polarization at the point I is known and equal to $\vec{P}_i$.

The component $\vec{P}_{i,\parallel}$, which is along $\hat{x}$ and parallel to $\vec{B}$, will be preserved while the component $\vec{P}_{i,\perp}$, which is along $\hat{y}$ and perpendicular to $\vec{B}$, will precess incoherently (due to magnetic field inhomogeneities) and will depolarize. Thus at the position II, as for the paramagnetic NSE, the recombination of the polarization components leads to two vectors: $\vec{P}_{i,\mathrm{NSE}} = (\vec{P}_{i,\parallel} - \vec{P}_{i,\perp})/2$ and $\vec{P}_{i,\mathrm{depol}} = (\vec{P}_{i,\parallel} + \vec{P}_{i,\perp})/2$. The former is mirror symmetric to $\vec{P}_i$ whereas the latter is equal to $\vec{P}_i/2$. If the polarization is not modified by the scattering at the sample, as it is the case for coherent nuclear scattering shown in Fig. 11A, $\vec{P}_{i,\mathrm{NSE}}$ will be the component that will satisfy the condition for echo while $\vec{P}_{i,\mathrm{depol}}$ will lead to a depolarized background.

Isotropic paramagnetic scattering will flip the component of the polarization along $\vec{Q}$ and as shown in Fig. 11B this flip introduces a phase shift of 180° for both $\vec{P}_{f,\mathrm{NSE}}$ and $\vec{P}_{f,\mathrm{depol}}$ with respect to the case of coherent nuclear scattering.

In the presence of chiral scattering this result must be complemented with the polarization created by the chiral correlations, which, as for the paramagnetic NSE, when averaged over all possible orientations of $\vec{P}_i$, leads to a reduced amplitude of the echo. On the other hand, similarly to paramagnetic NSE, for measurements on a position sensitive detector the chiral term introduces an overall phase shift of the echo group with respect to a reference (e.g. equatorial) plane.

Besides the similarities, there is a substantial difference between the paramagnetic and the ferromagnetic NSE (including all other methods using the four $\pi/2$ configuration such as polarimetric and intensity modulated NSE), as in the latter case it is not possible to disentangle the magnetic part from but all other contributions to scattering (nuclear – coherent and spin incoherent – and background). Thus, it is very difficult to extract reliable information when the magnetic signal is weak with respect to the rest. This is a major drawback, which also applies for the MIEZE (Gähler et al., 1992) variant of resonant NSE and limits the applications to cases of strong magnetic diffuse scattering. MnSi is one of these exceptional cases due to intense ring of diffuse scattering that appears above T_C and is schematically shown in Fig. 3A. In this case it was possible to use ferromagnetic NSE and follow the evolution of the chiral fluctuating correlations as the ring of scattering weakens and the scattering concentrates along the magnetic field direction with increasing magnetic field up to B = 0.4 T (Pappas et al., 2017).

4.3 Quantum Mechanical description of NSE

Larmor precession results from the coherent superposition of the spin-"up" and spin-"down" eigenstates and is the basis of NSE spectroscopy, which can be seen as a longitudical, Ramsey or Talbot-Lau, interferometry method (Rauch and Werner, 2015). This implies that after the first $\pi/2$ flip (Fig. 8), where the polarization of the neutron beam along the magnetic field is zero, the transverse polarization components are finite. One may draw parallels between this state and the S=0 state of a triplet, where the spin is zero but the angular momentum finite, in contrast to the singlet S=0 state, where both the spin and the angular momentum are zero, and which would be the equivalent of an incoherently depolarized neutron beam.

An alternative approach is that of a Mach-Zehnder interferometer by (Felber et al., 1999; Golub et al., 1994) who coined it "semi-classical" as it involves classical trajectories for wave packets of the two spin eigenstates. These separate and recombine in time for NSE including the resonance variant of it (Gähler et al., 1992) or in space for Spin Echo SANS (SESANS)

(Bouwman et al., 2000; Pynn, 1980; Rekveldt, 1996, 2000). It is still a point of debate which of the two approaches catches correctly the physics of Larmor precession based methods, see e.g. (de Haan et al., 2014; McKay et al., 2024) in the "Quantum Mechanical world", i.e. before the measurement (at the analyser-detector system) and the collapse of the eigenfunction to its eigenstates.

The Mach-Zehnder interferometer or two eigenstates approach has been very successful in visualising the evolution of the precession phase and optimising complex setups such as the combination of NSE and triple-axis spectroscopy (TAS) (Habicht et al., 2003). However, we argue that this approach does not catch the full complexity of the Quantum Mechanical problem as the neutron spin is a more complex entity than its eigenvalues and cannot be reduced to them. From that point of view and as discussed below the precession picture considered here and in (Mezei, 1980), involving Quantum Mechanical expectation values, appears to be more correct.

The decomposition in eigenstates and wave packets implies that in NSE and SESANS the result depends on the spread of these wave packets, thus on beam characteristics, a feature that has not been confirmed experimentally. In addition, as explained below, this approach does not account for both the paramagnetic NSE and SESANS nor for the ferromagnetic NSE methods.

The interaction of a precessing neutron beam polarization with a magnetic sample (which takes place in the "Quantum Mechanical world") requires $\vec{Q}$ to be in the precession plane in order to have half of the magnetic scattering acting as a π flipper, as shown in Fig. 9. This feature has been confirmed for both the paramagnetic NSE and the paramagnetic SESANS (Grigoriev et al., 2007; Rekveldt et al., 2006). However, if the neutron spin were decomposed to its eigenvalues, which would then be along the precession magnetic field and thus perpendicular to $\vec{Q}$, following Eq. 12 a homogeneous distribution of the magnetic moments in the plane perpendicular to $\vec{Q}$ would have led to $\vec{P}_f = 0$. Thus, the magnetic scattering would have been depolarized leading to zero echo/modulation for both the paramagnetic NSE and SESANS cases. In addition, this decomposition cannot explain the difference between magnetic and spin incoherent scattering, as the latter only introduces a phase shift of π but does not act as a π flipper. We note that our approach here is complementary to the one of section IIIC, where by knowing $\vec{P}_i$ we deduced the topology of the magnetic moments in MnSi. Here, by knowing the distribution of the magnetic moments in the sample, we deduce the topology of the neutron beam polarisation. In both cases the conclusions do not involve any assumptions but are a direct consequence of the vector nature of the (dipole) interaction between the neutron beam polarization and a magnetic sample.

The two eigenstates approach also cannot explain why in the ferromagnetic NSE configuration the result depends only on the magnetic field integral between the first two and the second two $\pi/2$ flippers (see Fig. 8), but not on the magnetic field at the sample. In fact, following the argumentation line of

(Grigoriev et al., 2003), the additional flippers in the ferromagnetic NSE setup should affect substantially the outcome and lead to high order correlation functions, an assumption which would however violate Born's rule and was not confirmed experimentally (Franson, 2010; Sinha et al., 2010).

Over the last years the two eigenstates approach is gaining ground among the SESANS community. A notable example is the investigation of the effect of gravity on a neutron beam (de Haan et al., 2014) where a comparison between the two approaches was undertaken with no conclusive outcome. However, this work does provide an answer or at least a very important hint. Neutron beams bend under the influence of gravity, because neutrons are heavy particles. This bending was experimentally observed also in the setup of (de Haan et al., 2014) but is correctly taken into account only in the precession approach not the two eigenstates one, which thus implicitly assumed zero gravitational effect. In fact the effect of the beam separation in the two eigenstates, if relevant, would have been seen as a deviation between the experimental results and the precession approach, which however was not detectable.

To conclude, the robustness of both NSE and SESANS hints to the longitudinal Talbot-Lau type interferometer description. This also explains why similar results can be obtained without a polarized neutron beam but with slits and gratings, a feature that led A. Ioffe to suggest using moving gratings, in the form of rotating discs such as choppers, in a setup, which he named "Neutron Speed Echo". This device could be used in combination with high magnetic fields as an add-on for TAS instruments (Ioffe, 2003) for high resolution studies of magnetic excitations.

Finally, an interesting question concerns the transition from one description to the other, which is more relevant to SESANS where a longitudinal separation of beams (Stern Gerlach effect) takes place. Based on experiments with photons, this would occur when the separation between the beams is comparable to their size. Thus for a separation of some μm and a beam height of some mm, as achieved nowadays with SESANS, the effect should be negligible.

5 Conclusions

Polarized neutron scattering provides direct and unique insight on the topology of magnetic correlations. In addition, Larmor labelling such as in Neutron Spin Echo (NSE) spectroscopy allows for reaching the highest energy resolution in neutron scattering while maintaining a high intensity beam. However, only a small number of experts worldwide are nowadays using the full power of these techniques. We expect this to change as the new generation high brilliance sources and the developments in neutron optics and polarizing devices (Böni, 2008; Jullien et al., 2021; Petukhov et al., 2016) make polarized neutrons an attractive option on almost all neutron scattering instruments, including for inelastic scattering (Arbe et al., 2020). It is thus anticipated that polarized neutron options will be available on almost all neutron scattering instruments on an every-day basis as an easy to

use and transparent tool serving a broad scientific community. This ambitious goal relies on the existence of a broad knowledge of this field with emphasis in magnetism, where subtleties of the interaction with a polarized neutron beam, especially when it comes to magnetic chirality can easily be overlooked or misinterpreted. The general but simple expressions and considerations we have derived here pinpoint to the particularities of chiral magnetic scattering and can be easily used to plan experiments and interpret their outcome.

Acknowledgements

It is a pleasure to thank Elizabeth Blackburn, Wim Bouwman, Jane Brown, Georg Ehlers, Bela Farago, Sergey Grigoriev, Fankang Li, Feri Mezei, Roger Pynn, Theo Rekveldt, Ross Stewart and Ad van Well for stimulating discussions.

References

Arbe, A., Nilsen, G.J., Stewart, J.R., Alvarez, F., Sakai, V.G., Colmenero, J., 2020. Coherent structural relaxation of water from meso- to intermolecular scales measured using neutron spectroscopy with polarization analysis. Phys. Rev. Res. 2, 022015.

Bannenberg, L.J., Kakurai, K., Falus, P., Lelièvre-Berna, E., Dalgliesh, R., Dewhurst, C.D., Qian, F., Onose, Y., Endoh, Y., Tokura, Y., Pappas, C., 2017. Universality of the helimagnetic transition in cubic chiral magnets: small angle neutron scattering and neutron spin echo spectroscopy studies of FeCoSi. Phys. Rev. B 95 (14), 144433.

Baum, M., 2013. Neutron-Scattering Studies on Chiral Multiferroics (Ph.D. thesis). University of Cologne.

Blume, M., 1963. Polarization Effects in the Magnetic Elastic Scattering of Slow Neutrons. Phys. Rev. 130, 1670.

Böni, P., 2008. New concepts for neutron instrumentation. NIMA 586, 1–8.

Bouwman, W., Oossanen, M., Uca, O., Kraan, W., Rekveldt, M., 2000. Development of spin-echo small-angle neutron scattering. J. Appl. Crystall. 33, 767.

Brown, P.J., 2001. Polarised neutrons and complex antiferromagnets: an overview. Physica B 297, 198.

Brown, P.J., Forsyth, J., Tasset, F., 1998. A study of magnetoelectric domain formation in Cr_2O_3. J. Phys.: Condens. Matter 10, 663.

Brown, P.J., Forsyth, J., Leliévre-Berna, E., Tasset, F., 2002. Determination of the magnetization distribution in Cr_2O_3 using spherical neutron polarimetry. J. Phys.: Condens. Matter 14, 1957.

Chacon, A., Heinen, L., Halder, M., Bauer, A., Simeth, W., Mühlbauer, S., Berger, H., Garst, M., Rosch, A., Pfleiderer, C., 2018. Observation of two independent skyrmion phases in a chiral magnetic material. Nat. Phys. 1–7.

Dally, R.L., Ratcliff, W.D., Zhang, L., Kim, H.S., Bleuel, M., Kim, J.W., Haule, K., Vanderbilt, D., Cheong, S.W., Lynn, J.W., 2020. Magnetic phase transitions and spin density distribution in the molecular multiferroic system GaV_4S_8. Phys. Rev. B 102, 014410.

de Haan, V.O., Plomp, J., van Well, A.A., Rekveldt, M.T., Hasegawa, Y.H., Dalgliesh, R.M., Steinke, N.J., 2014. Measurement of gravitation-induced quantum interference for neutrons in a spin-echo spectrometer. Phys. Rev. A 89, 063611.

Dyadkin, V.A., Grigoriev, S.V., Menzel, D., Chernyshov, D., Dmitriev, V., Schoenes, J., Maleyev, S.V., Moskvin, E.V., Eckerlebe, H., 2011. Control of chirality of transition-metal monosilicides by the Czochralski method. Phys. Rev. B 84, 014435.

Lelièvre-Berna, E., 2024. www.ill.eu/users/support-labs-infrastructure/sample-environment/equipment/polarimetry/snp-simulations.

Farago, B., Mezei, F., 1986. Study of magnon dynamics in Fe near Tc by modified neutron spin echo techniques. Physica B 136, 627.

Felber, J., Gähler, R., Golub, R., Hank, P., Ignatovich, V., Keller, T., Rauch, U., 1999. Neutron Time Interferometry. Found. Phys. 29, 381.

Fert, A., Cros, V., Sampaio, J., 2013. Skyrmions on the track. Nat. Nanotechnol. 8 (3), 152–156.

Finger, T., Senff, D., Schmalzl, K., Schmidt, W., Regnault, L.P., Becker, P., Bohaty`, L., Braden, M., 2010a. Electric-field control of the chiral magnetism of multiferroic MnWO4 as seen via polarized neutron diffraction. Phys. Rev. B 81, 54430.

Finger, T., Senff, D., Schmalzl, K., Schmidt, W., Regnault, L.P., Becker, P., Bohatý, L., Braden, M., 2010b. Polarized-neutron-scattering studies on the chiral magnetism in multiferroic mnwo4. J. Phys.: Conference Series 211, 012001. https://api.semanticscholar.org/CorpusID:136693490.

Franson, J.D., 2010. Physics. Pairs rule quantum interference. Science 329, 396.

Frisch, O.R., von Halban, H., Koch, J., 1938. Some experiments on the magnetic properties of free neutrons. Phys. Rev. 53, 719.

Gähler, R., Golub, R., Keller, T., 1992. Neutron resonance spin echo-a new tool for high resolution spectroscopy. Phys. B: Condens. Matter 180, 899–902.

Golub, R., Gähler, R., Keller, T., 1994. A plane wave approach to particle beam magnetic resonance. Am. J. Phys. 62, 779.

Grigoriev, S.V., Chetverikov, Y.O., Syromyatnikov, A.V., Kraan, W.H., Rekveldt, M.T., 2003. Neutron-multiwave-interference experiments with many resonance coils. Rev. A 68, 033603.

Grigoriev, S.V., Chetverikov, Y.O., Zabenkin, V.N., Theo Rekveldt, M., van Dijk, N., 2007. Spin-echo small-angle neutron scattering study of the domain structure of an Ni layer on a Cu substrate. J. Appl. Crystall. 40, s111.

Grigoriev, S.V., Maleyev, S.V., Moskvin, E.V., Dyadkin, V.A., Fouquet, P., Eckerlebe, H., 2010. Crossover behavior of critical helix fluctuations in MnSi. Phys. Rev. B 81, 144413.

Grigoriev, S.V., Maleyev, S.V., Okorokov, A.I., Chetverikov, Y.O., Georgii, R., Böni, P., Lamago, D., Eckerlebe, H., 2005. Critical fluctuations in MnSi near T_c: A polarized neutron scattering study. Phys. Rev. B 72, 134420.

Grigoriev, S.V., Potapova, N.M., Siegfried, S.A., Dyadkin, V.A., Moskvin, E.V., Dmitriev, V., Menzel, D., Dewhurst, C.D., Chernyshov, D., Sadykov, R.A., Fomicheva, L.N., Tsvyashchenko, A.V., 2013. Chiral properties of structure and magnetism in $Mn_{1-x}Fe_xGe$ compounds: when the left and the right are fighting, who wins? Phys. Rev. Lett. 110, 207201.

Habicht, K., Golub, R., Gähler, R., Keller, T., 2003. Space-time view of neutron spin echo, correlation functions and phonon focusing. In: Mezei, F., Pappas, C., Gutberlet, T. (Eds.), Neutron Spin Echo Spectroscopy: Basics, Trends and Applications. Springer, Berlin Heidelberg.

Halpern, O., Johnson, M.H., 1939. On the magnetic scattering of neutrons. Phys. Rev. 55, 898.

Hamann, A., Lamago, D., Wolf, T., Löhneysen, H.V., Reznik, D., 2011. Magnetic blue phase in the Chiral Itinerant magnet MnSi. Phys. Rev. Lett. 107, 037207.

Hearmon, A.J., Fabrizi, F., Chapon, L.C., Johnson, R.D., Prabhakaran, D., Streltsov, S.V., Brown, P.J., Radaelli, P.G., 2012. Electric field control of the magnetic chiralities in ferroaxial multiferroic $RbFe(MoO_4)_2$. Phys. Rev. Lett. 108, 237201.

Holbein, S., 2016. Neutron Scattering Studies on Complex Magnetic Structures in Magnetoelectric Materials (Ph.D. thesis). University of Cologne.

Hutanu, V., Sazonov, A.P., Meven, M., Roth, G., Gukasov, A., Murakawa, H., Tokura, Y., Szaller, D., Bordács, S., Kézsmárki, I., Guduru, V.K., Peters, L.C.J.M., Zeitler, U., Romhányi, J.,

Náfrádi, B., 2014. Evolution of two-dimensional antiferromagnetism with temperature and magnetic field in multiferroic $Ba_2CoGe_2O_7$. Phys. Rev. B 89, 064403.

Ioffe A., 2003. In Neutron Spin Echo Spectroscopy: Basics,Trends and Applications (Editor: F. Mezei, C. Pappas and Th. Gutberlet, Springer Verlag, vol. LNP 601, p. 142.

Ishikawa, Y., Noda, Y., Uemura, Y.J., Majkrzak, C.F., Shirane, G., 1985. Paramagnetic spin fluctuations in the weak itinerant-electron ferromagnet MnSi. Phys. Rev. B 31, 5884.

Ishiwata, S., Okuyama, D., Kakurai, K., Nishi, M., Taguchi, Y., Tokura, Y., 2010. Neutron diffraction studies on the multiferroic conical magnet $Ba_{2M}g_2Fe_{12}O_{22}$. Phys. Rev. B 81, 174418.

Izyumov, Y.A., 1962. Theory of scattering of slow neutrons in magnetic crystals. Soviet Phys.-JETP 15, 1162.

Janoschek, M., et al., 2013b. Phys. Rev. B 87, 134407.

Janoschek, M., Garst, M., Bauer, A., Krautscheid, P., Georgii, R., Böni, P., Pfleiderer, C., 2013a. Fluctuation-induced first-order phase transition in Dzyaloshinskii-Moriya helimagnets. Phys. Rev. B 87 (13), 134407.

Janoschek, M., Klimko, S., Gähler, R., Roessli, B., Böni, P., 2007. Spherical neutron polarimetry with MuPad. Phys. B: Condens. Matter 397 (1), 125–130 ISSN 0921-4526.

Jullien, D., Petoukhov, A., Enderle, M., Thiery, N., Mouveau, P., Bengaard Hansen, U., Chevalier, P., Courtois, P., 2021. New design of a magnetic device for wide-angle XYZ polarization analysis PASTIS-3, from the concept to first tests with thermal neutrons. NIMA 1010, 165558.

Kindervater, J., Häussler, W., Janoschek, M., Pfleiderer, C., Böni, P., Garst, M., 2014. Critical spin-flip scattering at the helimagnetic transition of MnSi. Phys. Rev. B 89 (18), 180408.

Lelièvre-Berna, E., Bentley, P., Bourgeat-Lami, E., Thomas, M., Pappas, C., Kischnik, R., Moskvin, E., 2009. Spherical neutron polarimetry applied to spin-echo and time-of-flight spectroscopy. Physica B 404, 2624.

Lelièvre-Berna, E., Bourgeat-Lami, E., Fouilloux, P., Geffray, B., Gibert, Y., Kakurai, K., Kernavanois, N., Longuet, B., Mantegezza, F., Nakamura, M., Pujol, S., Regnault, L.-P., Tasset, F., Takeda, M., Thomas, M., Tonon, X., 2005. Advances in spherical neutron polarimetry with Cryopad. Physica B 356, 131.

Lelièvre-Berna, E., Brown, P.J., Tasset, F., Kakurai, K., Takeda, M., Regnault, L.-P., 2007. Precision manipulation of the neutron polarisation vector. Physica B 397, 120.

Maleyev, S.V., Bar'yakhtar, V.G, .Suris, R.A., 1962. The scattering of slow neutrons by complex magnetic structures. Fiz. Tv. Tela 44, 3461.

Maleyev, S.V., Bar'yakhtar, V.G., Suris, R.A., 1963. The scattering of slow neutrons by complex magnetic structures. 1962. .Sov. Phys. Solid State 4, 2533.

Marty, K., Simonet, V., Ressouche, E., Ballou, R., Lejay, P., Bordet, P., 2008. Single domain magnetic helicity and triangular chirality in structurally enantiopure $Ba_3NbFe_3Si_2O_{14}$. Phys. Rev. Lett. 101, 247201.

McKay, S., Irfan, A.A.M., Le Thien, Q., Geerits, N., Parnell, S.R., Dalgliesh, R.M., Lavrik, N.V., Kravchenko, I.I., Ortiz, G., Pynn, R., 2024. Experimental evidence for the two-path description of neutron spin echo. Phys. Rev. A 109, 042420.

Mezei, F., 1980. Imaging processes and coherence in physics. Lecture Notes in Physics. 112. Springer, Verlag, pp. 279 (LNP, volume 112).

Mezei, F., 1980. Neutron spin echo. Lecture Notes in Physics Springer Vrrlag.

Mezei, F., Pappas, C., Gutberlet, T., 2003. Neutron spin echo spectroscopy basics, trends and applications. Lecture Notes in Physics. Springer Verlag, Berlin, pp. 601.

Moskvin, E., Grigoriev, S., Dyadkin, V., Eckerlebe, H., Baenitz, M., Schmidt, M., Wilhelm, H., 2013. Chiral Modulations in FeGe Close to Magnetic Ordering. Phys. Rev. Lett. 110, 077207 Complex.

Murani, A.P., Mezei, F., 1980. Neutron spin echo. Lecture Notes in Physics Springer, Verlag.

Overhauser, A.W., 1962. Polarization of Neutrons by Diffraction from a Helical Antiferromagnet. Bull. Am. Phys. Soc. 7, 241.

Pappas, C., Bannenberg, L.J., Lelièvre-Berna, E., Qian, F., Dewhurst, C.D., Dalgliesh, R., Schlagel, D., Lograsso, T., Falus, P., 2017. Magnetic fluctuations, precursor phenomena, and phase transition in MnSi under a magnetic field. Phys. Rev. Lett. 119 (4), 047203.

Pappas, C., Lelièvre-Berna, E., Bentley, P., Bourgeat-Lami, E., Moskvin, E., Thomas, M., Grigoriev, S., Dyadkin, V., 2008. Polarimetric neutron spin echo: Feasibility and first results. Nucl. Inst. Methods Phys. Res. A 592, 420.

Pappas, C., Lelièvre-Berna, E., Falus, P., Farago, B., Bentley, P., Moskvin, E., Krist, T., Grigoriev, S., 2009. Challenges in neutron spin echo spectroscopy. Physica B 592, 2578.

Pappas, C., Lelièvre-Berna, E., Falus, P., Bentley, P.M., Moskvin, E., Grigoriev, S., Farago, B., 2009. Chiral Paramagnetic Skyrmion-like Phase in MnSi. Phys. Rev. Lett. 102, 197202.

Pappas, C., Lelièvre-Berna, E., Fouquet, P., Falus, P., Farago, B., 2011. Magnetic fluctuations and correlations in MnSi: Evidence for a chiral skyrmion spin liquid phase. Phys. Rev. B. 102, 197202.

Pappas, C., Leonov, A.O., Bannenberg, L.J., Fouquet, P., Wolf, T., Weber, F., 2021. Evolution of helimagnetic correlations when approaching the quantum critical point of $Mn_{1-x}Fe_xSi$. Phys. Rev. Res. 3, 013019.

Petukhov, A., Nesvizhevsky, V., Bigault, T., Courtois, P., Jullien, D., Soldner, T., 2016. A concept of advanced broad-band solid-state supermirror polarizers for cold neutrons. NIMA 838, 33–38.

Pynn, R., 1980. In: Mezei, F. (Ed.), Neutron Spin Echo. Lecture Notes in Physics 128 Springer Verlag.

Qian, F., Bannenberg, L.J., Wilhelm, H., Chaboussant, G., DeBeer-Schmitt, L.M., Schmidt, M.P., Aqeel, A., Palstra, T.T.M., Brück, E.H., Lefering, A.J.E., Pappas, C., Mostovoy, M., Leonov, A.O., 2018. New magnetic phase of the chiral skyrmion material Cu_2OSeO_3. Sci. Adv. 4, eaat7323.

Rauch, H., Werner, S.A., 2015. Neutron Interferometry: Lessons in Experimental Quantum Mechanics, Wave- Particle Duality, and Entanglement. Oxford University Press.

Rekveldt, M., 1996. Novel sans instrument using neutron spin echo. NIMA 114, 366.

Rekveldt, M., 2000. Novel instrumentation concepts using polarised neutrons. Phys. B Phys. Cond. Matter 276, 55.

Rekveldt, M.T., van Dijk, N.H., Grigoriev, S.V., Grigoriev, S.V., Kraan, W.H., Bouwman, W.G., 2006. Three-dimensional magnetic spin-echo small-angle neutron scattering and neutron depolarization: A comparison. Rev. Sci. Instrum. 77, 073902.

Rodríguez-Velamazán, J.A., Fabelo, O., Campo, J., et al., 2018. Switching of the chiral magnetic domains in the hybrid molecular/inorganic multiferroic $(ND_4)_2[FeCl_5(D_2O)]$. Sci. Rep. 8, 10665.

Roessli, B., Böni, P., Fischer, W.E., Endoh, Y., 2002. Chiral fluctuations in MnSi above the Curie temperature. Phys. Rev. Lett. 88, 237204.

Sampaio, J., Cros, V., Rohart, S., Thiaville, A., Fert, A., 2013. Nucleation, stability and current-induced motion of isolated magnetic skyrmions in nanostructures. Nat. Nanotechnol. 8 (11), 839–844.

Simonet, V., Loire, M., Ballou, R., 2012. Magnetic chirality as probed by neutron scattering. Eur. Phys. J. Special Topics 213, 5.

Sinha, U., Couteau, C., Jennewein, T., Laflamme, R., Weihs, G., 2010. Ruling out multi-order interference in quantum mechanics. Science 329, 418.

Stewart R.J. Experimentally tested on the IN11 NSE spectrometer of the Institut Laue Langevin Grenoble, France.

Tasset, F., 1989. Zero field neutron polarimetry. Physica B 156–159, 627.

Yamasaki, Y., Sagayama, H., Goto, T., Matsuura, M., Hirota, K., Arima, T., Tokura, Y., 2007. Electric control of spin helicity in a magnetic ferroelectric. Phys. Rev. Lett. 98, 147204.